PHYSICAL REVIEW E **106**, 025203 (2022)

Ultrahigh-amplitude isolated attosecond pulses generated by a two-color laser pulse interacting with a microstructured target

Shengzhan Wei,[1] Yunliang Wang,[1,*] Xueqing Yan,[2,3,4,†] and Bengt Eliasson[5,‡]

[1]*Department of Physics, School of Mathematics and Physics, University of Science and Technology Beijing, Beijing 100083, China*
[2]*State Key Laboratory of Nuclear Physics and Technology, and Key Laboratory of HEDP of the Ministry of Education, CAPT, Peking University, Beijing 100871, China*
[3]*Beijing Laser Acceleration Innovation Center, Beijing 100871, China*
[4]*Collaborative Innovation Center of Extreme Optics, Shanxi University, Shanxi 030006, China*
[5]*SUPA, Physics Department, John Anderson Building, University of Strathclyde, Glasgow G4 0NG, Scotland*

(Received 29 November 2021; accepted 26 July 2022; published 15 August 2022)

A unique electron nanobunching mechanism using a two-color laser pulse interacting with a microstructured foil is proposed for directly generating ultraintense isolated attosecond pulses in the transmission direction without requiring extra filters and gating techniques. The unique nanobunching mechanism ensures that only one electron sheet contributes to the transmitted radiation. Accordingly, the generated attosecond pulses are unipolar and have durations at the full width at half-maximum about 5 attoseconds. The emitted ultrahigh-amplitude isolated attosecond pulses have intensities of up to $\sim 10^{21}\ \mathrm{W/cm^2}$, which are beyond the limitations of weak attosecond pulses generated by gas harmonics sources and may open a new regime of nonlinear attosecond studies. Unipolar pulses can be useful for probing ultrafast electron dynamics in matter via asymmetric manipulation.

DOI: 10.1103/PhysRevE.106.025203

I. INTRODUCTION

Ultrafast optics has developed rapidly recently due to the huge potential of probing the ultrafast dynamics of electrons in matter [1]. Half-cycle pulses, or unipolar pulses [2], may be useful for probing electron dynamics in solids and atoms by asymmetrical manipulation [3–6]. Recent advances have allowed for the generation of intense attosecond pulses using high-order harmonic generation (HHG) by the dense electron sheet in wakefield acceleration [7], or through the nonlinear interaction of intense laser pulse with solid targets with different mechanisms, such as coherent wake emission (CWE) [8,9], relativistic oscillating mirror (ROM) [10–14], and coherent synchrotron emission (CSE) [15–17]. An advantage of the CSE mechanism is that the intensity of the generated attosecond pulse is much higher than that of the incident pulse and the attosecond pulses can be emitted in the transmission direction of the incident laser pulse. Moreover, there is no strict limitation on the amplitude of the incident pulse in the CSE regime. In the relativistic regime of HHG, the higher laser intensities induce stronger nonlinearities giving rise to higher-harmonic efficiency.

In the CSE regime, the formation and dynamics of extremely dense electron sheet is crucial for the emission of attosecond pulses [15]. A multicycle laser pulse interacting with a solid target usually emits a train of attosecond pulses. However, for many applications of pump-probe techniques an isolated attosecond pulse is preferred. One way to produce an isolated attosecond pulse is to use polarization gating [18,19]. The combination of polarization and ionization gating and the spatial propagation effects was proposed for generating single isolated attosecond pulses [20,21], which was later experimentally demonstrated [22]. An isolated attosecond pulses can be produced by a two-color multicycle laser pulse interacting with a nanometer scale foil [23]. The two-color laser pulses are useful for enhancing the attosecond extreme ultraviolet (EUV) yield [24–28]. Another way of producing isolated attosecond pulse is to use a few-cycle laser pulse interacting with a foil [29]. Recently, the direct generation of an isolated attosecond pulse was suggested by using a 2.5-cycle laser [5] or a 0.5-cycle laser [6] in the transmission direction. However, when a one-cycle laser pulse is interacting with solid target, a secondary electron nanobunch will be formed in addition to the primary electron sheet formed in the first half cycle of the laser. This results in that the generated attosecond pulse has a structure of two distinct subpulses, with higher frequencies emitted by the primary electron bunch and lower frequencies by the secondary bunch [30].

In this paper, we propose a unique CSE regime that ensures only one electron sheet contributing to the transmitted radiation, where the microstructured target is crucial for this unique regime. We show that a normalized areal charge density of the first target layer plays an important role for the dynamics of the electron sheet. If the density and thickness of the first layer target change simultaneously to ensure that the normalized areal charge density is unchanged, the electrodynamics of the electron sheet will remain unchanged and attosecond pulse generation is effective in this CSE regime.

---

[*] ylwang@ustb.edu.cn
[†] x.yan@pku.edu.cn
[‡] bengt.eliasson@strath.ac.uk

©2022 American Physical Society

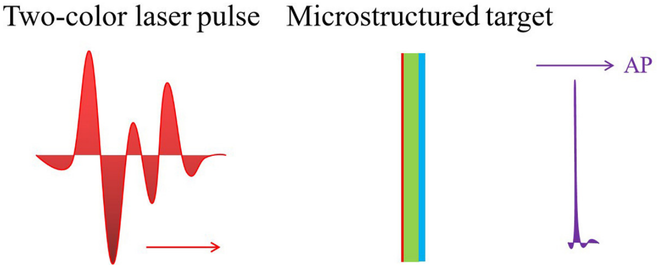

FIG. 1. Schematic of an attosecond pulse (AP) generated by the interaction of a two-color laser pulse with a microstructured foil.

II. EMISSION OF THE ISOLATED ATTOSECOND PULSE

Here, a unique electron nanobunching mechanism is proposed, in which a two-color laser pulse interacting with a microstructured foil can directly generate ultraintense isolated attosecond pulses in the transmission direction. The schematics of a two-color laser pulse interacting with a microstructured foil to generate attosecond pulses is illustrated in Fig. 1. The microstructured target has a sandwich-like structure with three layers. A linearly polarized (along z) two-color laser pulse is launched in the x direction, normally incident on the microstructured foil. An ultraintense isolated attosecond pulses in the transmission direction is generated without the need for extra filters and gating techniques. The technique ensures that only one electron sheet contributes to the transmitted radiation. The formation and dynamics of the electron sheet is controlled by adjusting the relative phase between the two frequency components of the two-color laser pulse.

We used the particle-in-cell (PIC) code EPOCH [31] to perform simulations to study the interaction and optimize relevant parameters. The wavelength of the fundamental frequency laser pulse is $\lambda_L = 800\,\mathrm{nm}$ with the angular frequency being $\omega_1 = \omega_L = 2\pi c/\lambda_L$ and the period being $T_L = \lambda_L/c = 2.67$ femtoseconds. The second harmonic laser pulse has an angular frequency $\omega_2 = 2\,\omega_L$. The two-color laser pulse has a normalized electric field $a_z = eE_L/(\omega_L m_e c)$ of the form $a_z = a_1 + a_2$, where E_L is the electric field amplitude of the laser pulse, m_e is the electron rest mass, e is the unit charge charge, and c is the speed of light in a vacuum. The two-color laser pulse has a Gaussian temporal envelope given by $a_{1,2} = a_{01,02} e^{-(t-T_L)^2/\tau^2} \sin[\omega_{1,2}(t - T_L) + \phi_{1,2}]$, where $\phi_1 = 5.055$ rad and $\phi_2 = 9.200$ rad are the phases of the fundamental and second harmonic frequency laser pulses, respectively. Here, $\tau = 0.5\,T_L$ is related to the duration $\sqrt{2\ln(2)}\tau = 0.59\,T_L$ of the two-color laser pulse. The normalized amplitudes of the fundamental and second harmonic pulses are $a_{01} = 40.0$ and $a_{02} = 44.4$, respectively. The corresponding intensities are $3.42 \times 10^{21}\,\mathrm{W/cm^2}$ and $4.22 \times 10^{21}\,\mathrm{W/cm^2}$ of the fundamental and second harmonic pulses, respectively. The length of the one-dimensional simulation box is $8\,\lambda_L$, which is resolved by 10 000 cells per wavelength. The microstructured target has a sandwich-like structure with three layers. The first layer is an ultrathin plasma film, located in the region $5\,\lambda_L < x < 5.0025\,\lambda_L$ with high number density $n_{e1} = 950\,n_c$, where the critical number density is $n_c = \omega_L^2 \epsilon_0 m_e/e^2 \sim 1.74 \times 10^{27}/\mathrm{m}^3$ with ϵ_0 being the electric permittivity in vacuum. The second layer is at $5.0025\,\lambda_L < x < 5.315\,\lambda_L$ with number density $n_{e2} = 50\,n_c$. The third layer is at $5.315\,\lambda_L < x < 5.3525\,\lambda_L$ with density $n_{e3} = 150\,n_c$. The third target acts mainly as a high-pass filter to prevent low frequency harmonics from being transmitted in the transmission direction. We assume that the ions remain stationary on the short timescale of the few-cycle laser pulses.

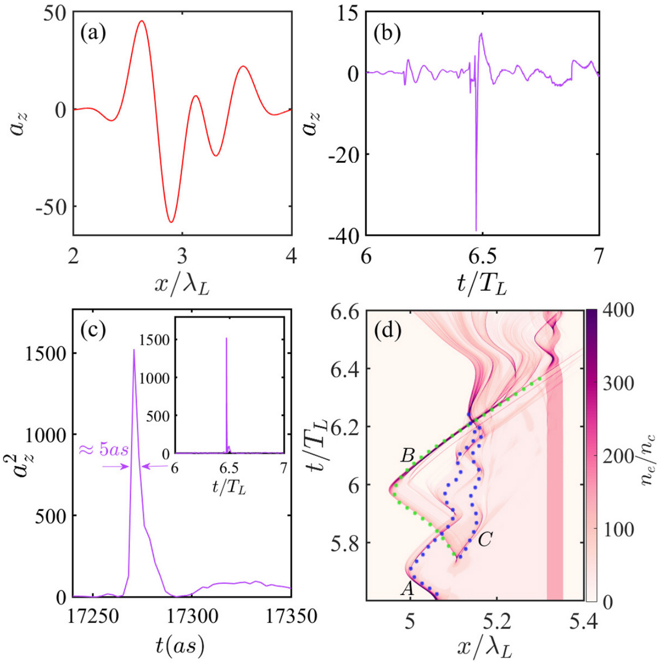

FIG. 2. (a) The spatial profile of normalized electric field $a_z = eE_z/(\omega_L m_e c)$ of the driving two-color laser pulses. (b) The normalized electric field of an attosecond pulse in transmission direction. (c) A close-up of the attosecond pulse showing a FWHM of about 5 as. The inset shows the profile of the intensity of the attosecond pulse. (d) The spatiotemporal evolution of the normalized electron number density n_e/n_c. The trajectory of electron sheet B is marked by a green dotted line and the trajectory of electron sheets A and C are represented by blue dotted lines.

The profile of the two-color driving laser pulse is shown in Fig. 2(a). As seen in Fig 2(b), the attosecond pulse is approximately a half-cycle pulse. As seen in Fig. 2(c), an ultrahigh amplitude isolated attosecond pulse is emitted with a squared amplitude of $a_z^2 \approx 1500$ and a corresponding intensity of $3.2 \times 10^{21}\,\mathrm{W/cm^2}$. The full width at half maximum (FWHM) of the attosecond pulse is about 5 as. Although the attosecond pulse is emitted by the electron sheet B mainly coming from the second target layer as can be seen in Fig. 2(d), the presence of the first target layer plays a crucial role for the emission of the isolated attosecond pulse in the transmission direction. Because of the presence of the first target layer with very high density, the fundamental frequency laser pulse by itself is not enough to form a high-density electron sheet. It is necessary to introduce the second harmonic laser pulse to reduce the oscillation period of the transverse electric field and increase the Lorentz force, which contributes to the formation of the electron sheet B propagating in the transmission direction.

The generation region of the isolated attosecond pulse is shown in Fig. 2(d). When the two-color laser pulse impinges

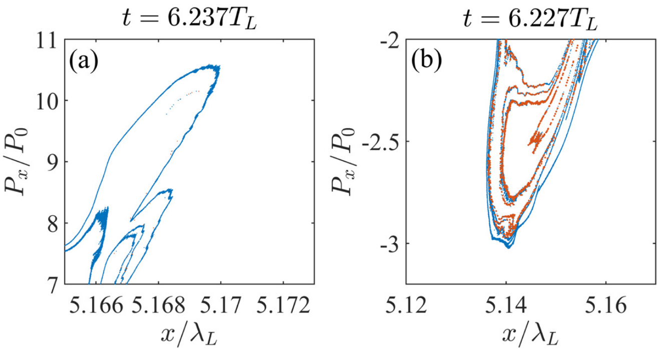

FIG. 3. (a) The longitudinal momentum distribution of the electron sheet B at $t = 6.237\,T_L$. (b) The longitudinal momentum distribution of the reverse moving electron sheet A and C at $t = 6.227\,T_L$ after the intersection point. The three electron sheets intersect at $t = 6.216\,T_L$. Red color indicates electrons from the first target layer and blue color electrons from the second target layer. Momentum $P_x = \gamma m_e v_x$ is normalized by $P_0 = m_e c$.

normally onto the surface of the target, the electrons are compressed by the laser ponderomotive force to form the electron sheet A, which is formed mainly from the electrons in the first target layer. When the electron sheet A moves towards the bulk plasma, a transient longitudinal electrostatic field is created due to the charge separation. As a result, the electron sheet A is accelerated backwards to the reflected direction. After that, the secondary electron sheets B and C are simultaneously formed, the electrons of which are mainly from the second layer. Under the combined action of the Coulomb and Lorentz forces, the electron sheet A keeps oscillating and moves into the bulk plasma, which results in an ultrahigh positive charge density in the vicinity of the first target layer due to the presence of the high-density first layer. Accordingly, the Coulomb and Lorentz forces are strong enough to prevent almost all of the electrons in the electron sheet B from escaping to the vacuum to be lost. Instead, the electron sheet B is returned back to the transmission direction as shown by the green dotted line in Fig. 2(d). When the electron bunch B passes through the left boundary of the target, the Lorentz force $\sim\mathbf{v} \times \mathbf{B}$ of the driving two-color laser pulse can continue to accelerate the electron sheet B, which is a benefit from the proper waveform interacting with the foil, which can be achieved by adjusting the relative phase between the two-color laser pulses. On the other hand, the electron sheets A and C keep serrated oscillating in the bulk plasma and eventually merge to form a high-density electron nanobunch, which is illustrated by the blue dotted line in Fig. 2(d). This later intersects with the electron sheet B at time $t = 6.216\,T_L$. After that, the combined electron sheets A and C will move in the reflection direction and have a reverse momentum compared to electron sheet B, which is confirmed by the dynamics of the electron sheets A, C, and B in the phase space in Fig. 3. Figure 3(a) shows that electron sheet B mainly originates from the second target layer, where the momentum distribution takes the shape of a whip. Figures 3(a) and 3(b) show that the longitudinal momentum of the backward-propagating combined electron sheets A and C is smaller than that of the forward propagating electron sheet B after their intersection.

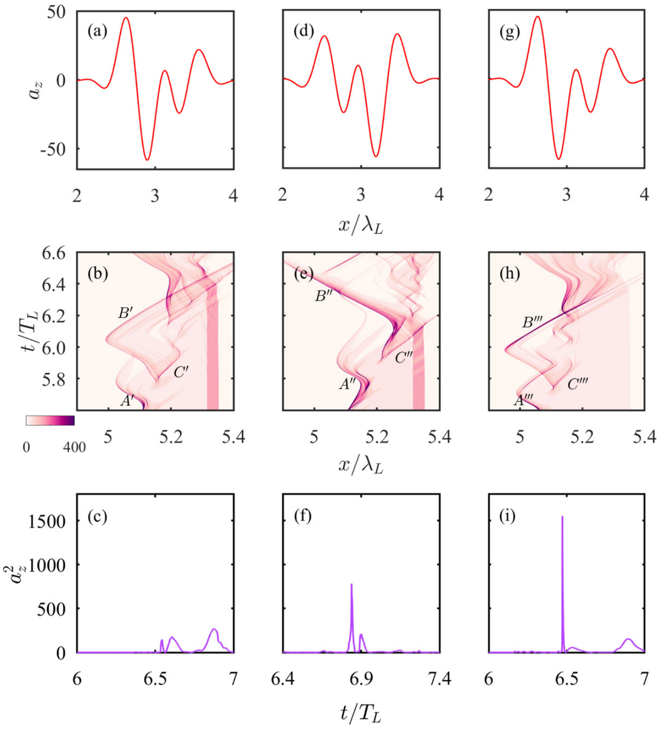

FIG. 4. Left column: Attosecond pulse generation without the first target layer while keeping other parameters unchanged. Middle column: Attosecond pulse generation without the first target layer while optimizing the relative phase ($\phi_1 = 5.055$ rad, $\phi_2 = 7.600$ rad) between the two-color laser pulses. Right column: Attosecond pulse generation without the third target layer while keeping other parameters unchanged. The first row shows the spatial profile of normalized electric field $a_z = eE_z/(\omega_L m_e c)$ of the driving two-color laser pulses for the three cases. The second row gives spatiotemporal evolution of the normalized electron number density n_e/n_c for the three cases. The third row illustrates the generation of attosecond pulse in the transmission direction without filtering for the three cases.

Accordingly, the electron sheets A and C do not contribute to the emission of the attosecond pulse in the transmission direction. The attosecond pulse in the transmission direction is mainly emitted by the electron bunch B.

III. PHYSICAL MECHANISM OF MICROSTRUCTURED TARGET

Even though the transmitted attosecond pulse is produced by the second target layer, the first target layer plays an important role. Figure 4 shows the result in the absence of the first target layer but keeping the other parameters the same as in Fig. 2. As seen in Figs. 4(a), 4(b), and 4(c), the same two-color laser pulse incident on the target produces only a low amplitude attosecond pulse, followed by two broad subpulses. The ponderomotive force of the two-color laser pulse is too strong, the electron sheets A' and C' in Fig. 4(c) quickly spread out in space, and other secondary electron sheets are formed at time $t = 6.017T_L$ and $t = 6.149T_L$. Because there is no high density first layer, the Coulomb force is not strong enough to make the electron sheets A' and other secondary electron sheets to move in the opposite direction. As a result, the transmitted radiation is emitted by too many electron sheets and is no longer an isolated pulse, as seen in Figs. 4(b) and 4(c).

Even if the phases of the two laser pulses are optimized, as shown in Figs. 4(d), 4(e), and 4(f), with $\phi_1 = 5.055$ rad and $\phi_2 = 7.600$ rad giving the optimized waveform plotted in Fig. 4(d), the intensity of the attosecond pulse illustrated in Fig. 4(f) is lower than that in the presence of the first target layer, and there is an additional subpulse after the main pulse. The spatiotemporal evolution of the electron number density in Fig. 4(e) shows that the electron sheet B'' is accelerated in the reflected direction and escape to a vacuum. Only a portion of the backward electron sheet B'' returns back to the transmission direction to emit the attosecond pulse, which reduces the intensity of the attosecond pulse in the transmission direction.

The third target layer acts mainly as a high-pass filter to prevent low frequency harmonics from being transmitted in the transmission direction. From Fig. 2(d), we can clearly see that the formation of electron sheet B is not related to the third target layer. Figures 4(g), 4(h), and 4(i) illustrate the result in the absence of the third target layer, but keeping the other parameters the same as in Fig. 2 except that the thickness of the second target layer is increased by 30 nm. We can see that the dynamics of the formation of electron sheets B''', A''', and C''' are almost the same as the previous case in that the third target layer is present shown in Fig. 2(d). The electron sheet B''' is formed by the second target layer and is responsible for the emission of the forward attosecond pulse. The intensity of the forward attosecond pulse illustrated in Fig. 4(i) is slightly larger than the previous case with the third target layer, which is due to the fact that there is no high-pass filter effect as the third target layer is absent. The minor disadvantage of no third layer target is that a subpulse with very low intensity appears far away from the main pulse.

IV. PHYSICAL MECHANISM OF THE TWO-COLOR LASER PULSE

We here discuss the physical mechanism of the two-color laser pulse with parallel or orthogonal linear polarization. The unique waveform of the two-color laser pulse is different to the one-color laser pulse and is crucial for the generation of the forward attosecond pulse. As the waveform is heavily affected by the relative phase and energy ratio, we made simulations with various energy ratios $\eta = a_1^2/a_0^2$, where $a_0^2 = a_{01}^2 + a_{02}^2$ and $a_{01,02}$ is the same as that in Fig. 2. The fundamental ($\lambda_L = 800$ nm) and second harmonic frequency ($\lambda_L = 400$ nm) laser pulses are all linearly polarized in the z direction. The two-color laser pulse has a Gaussian temporal envelope given by $a_{z1} = a_1 e^{-(t-T_L)^2/\tau^2} \sin[\omega_L(t - T_L) + \phi_1]$ and $a_{z2} = a_2 e^{-(t-T_L)^2/\tau^2} \sin[2\omega_L(t - T_L) + \phi_2]$ for the fundamental and second harmonic frequency laser pulses, respectively. Here $a_1 = \sqrt{\eta} a_0$ and $a_2 = \sqrt{1-\eta} a_0$. The other parameters ϕ_1, ϕ_2, and τ are the same as in Fig. 2. In Fig. 5(a), the forward attosecond pulses are generated for a range of energy ratioa $\eta \sim 0.3$–0.7. We obtained the optimized parameter $\eta = 0.448$ and found that the amplitude and duration of the attosecond pulses are $a_z \sim 39$ and 5 as in Fig. 2(c). When the energy ratio of the fundamental frequency wave and second harmonic wave is nearly equal, the forward attosecond pulses are all isolated pulses as shown in Fig. 5(a). We also investigate the effects of the relative phase in the case of optimal energy ratio $\eta = 0.448$ in Fig. 5(b), where we fixed the phase of the fundamental frequency laser $\phi_1 = 5.055$ rad and changed the phase ϕ_2 of the second harmonic frequency laser pulse, which shows that with the change of phase $\Delta\phi = \phi_2 - 9.2$ rad, the duration at the FWHM of the attosecond pulses are all below 10 as and the intensity $a_z^2 > 400$ for $-0.2\ \text{rad} < \Delta\phi < 0.8$ rad.

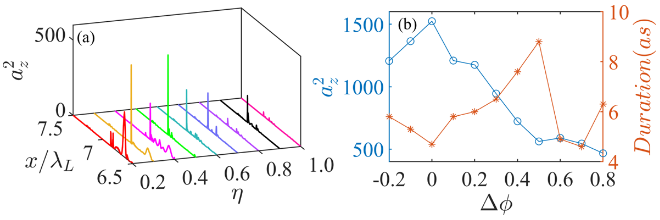

FIG. 5. (a) The forward attosecond pulse is illustrated for different energy ratios η. (b) Durations (as) at FWHM and normalized intensities a_z^2 of the attosecond pulses as functions of the change of phase $\Delta\phi$ of the second harmonic frequency laser in the case of optimal energy ratio $\eta = 0.448$.

The generation regime of the forward attosecond pulse can be understood by studying the spatiotemporal evolution of the electron number density shown in Fig. 6. For a range of an energy ratios $\eta \sim 0.3$–0.7 shown in Figs. 6(b) to 6(f), the electron sheets are formed mainly from the second target layer and their trajectories are marked by blue dotted lines. As the electrons from the first target layer are oscillating and move into the bulk plasma, an ultrahigh positive charge density in the vicinity of the first target layer is formed due to the presence of the high-density first layer. Accordingly, the Coulomb and Lorentz forces are strong enough to make the electron sheet return back to the transmission direction. Then the forward attosecond pulses are generated by the electrons' sheets when they are accelerated by the Lorentz force of the driving two-color laser pulse, which benefits from the proper waveform interacting with the foil. One can conclude that the mechanism of the forward attosecond pulse generation is similar for a wide range of energy ratios.

If the energy ratio is too small, the second harmonic laser pulse will dominate in the laser plasma interaction. Accordingly the period of electron oscillation is shortened and the oscillation times also increases, which results in more than one electron sheet propagating in the transmitted direction as shown in Fig. 6(a). Then the forward attosecond pulses [shown by the red line in Fig. 5(a) at $\eta = 0.2$] are not isolated pulses but pulse trains. While the energy ratio is too large, the fundamental frequency laser pulse will dominate in the forward radiation. In the case of $\eta = 1$, the fundamental frequency laser pulse is only considered. The results in Fig. 6(i) show that the electron sheet (marked by the black dotted line) from the second target layer will not accelerate in the transmitted direction, but return back to the reflected direction. Although there is electron sheet (marked by the green dotted line) from first target layer propagating to transmitted direction, the forward radiation is very weak as the electron density is not large enough.

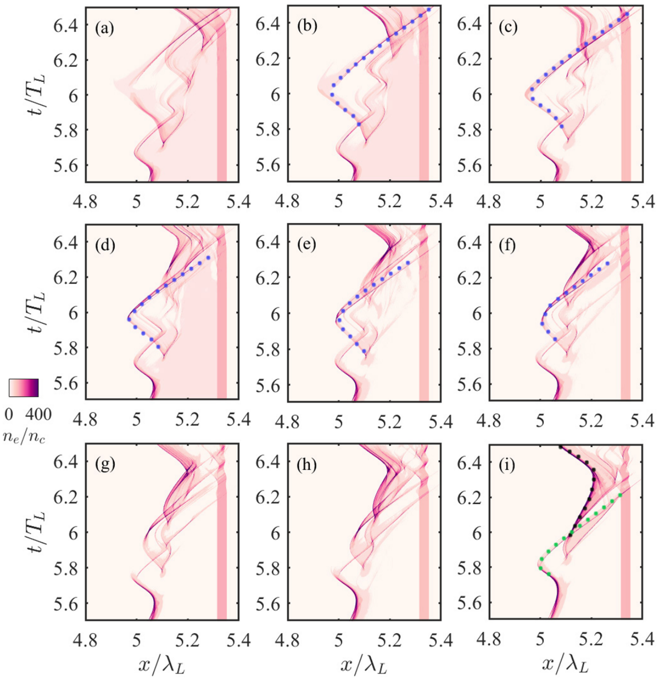

FIG. 6. The spatiotemporal evolution of the normalized electron number density n_e/n_c for different energy ratio: (a) $\eta = 0.2$, (b) $\eta = 0.3$, (c) $\eta = 0.4$, (d) $\eta = 0.5$, (e) $\eta = 0.6$ (f) $\eta = 0.7$, (g) $\eta = 0.8$ (h) $\eta = 0.9$, and (i) $\eta = 1$. The trajectory of electron sheet responding for forward attosecond pulse emission is marked by a blue dotted line in (b)–(f). Panel (i) shows the case where only the fundamental frequency laser exists. The black dotted line in (i) illustrates the electron sheet from the second target layer and the green dotted line is referred to as the electron sheet from the first target layer.

We considered the polarization degree effects on the generation of the forward attosecond pulse in Fig. 7. The fundamental frequency laser pulse is linearly polarized along z and the second harmonic frequency laser pulse is linearly polarized and along y. To consider the effects of energy ratio, the Gaussian temporal envelope is given by $a_{z1} = \sqrt{\eta}a_0 e^{-(t-T_L)^2/\tau^2}\sin[\omega_L(t - T_L) + \phi_1]$ and $a_{y2} = \sqrt{1-\eta}a_0 e^{-(t-T_L)^2/\tau^2}\sin[2\omega_L(t - T_L) + \phi_2]$ for the fundamental and second harmonic frequency laser pulses, respectively, which have the same phases $\phi_1 = \phi_2 = 5.055$ rad. The simulation results show that the forward attosecond pulse can be radiated when the energy ratio is larger than ~0.9 as shown in Figs. 7(a) and 7(b), where the forward attosecond pulse is illustrated and the waveform is like the elliptic polarization. If the energy ratio is smaller than 0.9, the attosecond pulse is no longer radiated. To consider the relative phase effects on attosecond pulse generation, we fixed the energy ratio $\eta = 0.9$ and the phase of the fundamental frequency laser $\phi_1 = 5.055$ rad and changed the phase ϕ_2 of the second harmonic frequency laser pulse. The simulation results are illustrated in Figs. 7(c) and 7(d) $\delta\phi = 0.01$, 7(e) and 7(f) $\delta\phi = 0.02$, 7(g) and 7(h) $\delta\phi = 0.03$, which show that the amplitude of the attosecond pulse decreases with the increase of the relative phase $\delta\phi$.

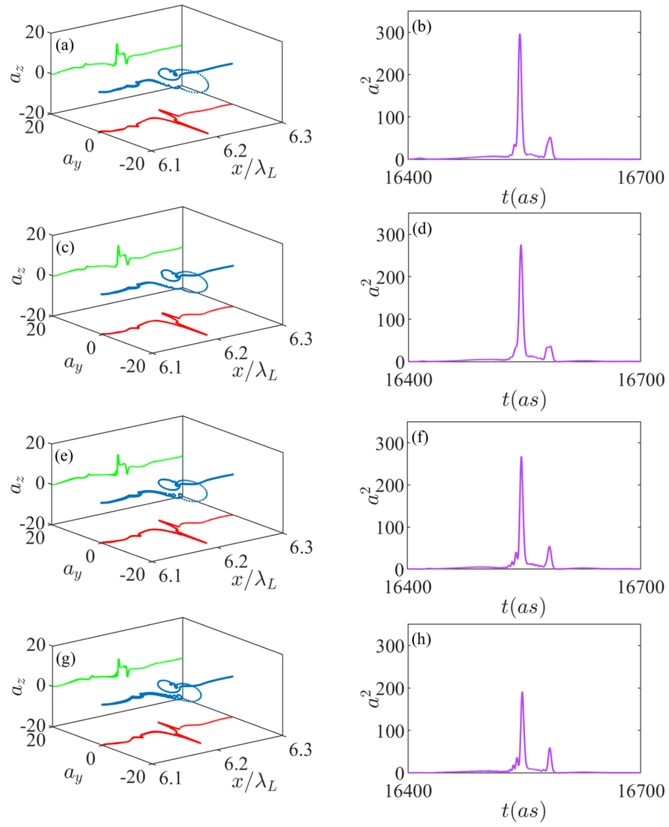

FIG. 7. The forward attosecond pulse generation from the interaction of two orthogonal linear polarization laser pulses with the microstructured target with different relative phase as (a,b) $\delta\phi = 0$, (c,d) $\delta\phi = 0.01$, (e,f) $\delta\phi = 0.02$, (g,h) $\delta\phi = 0.03$. The left column is the electric field amplitude of the attosecond pulse. The right column is the intensity of attosecond pulse.

V. THEORETICAL MODEL OF FORWARD EMISSION

The emission process of the attosecond pulse can be analyzed by the stationary phase method (SPM), in which it is assumed that the HHG depends largely on the behavior of the electrons at the stationary phase point (SPP) [15]. Figure 8(a) shows the SPP of the transverse current distribution of electron sheet *B* marked with a green dot, where the electron sheet *B* has an ultrarelativistic longitudinal velocity with $\gamma \approx 10$ and the transverse velocity is close to zero. Because of the trajectory crossing, where three electron sheets *A*, *C*, and *B* meet, the electron sheets *A* and *C* has a shielding effect on the electrostatic field a_x due to the background positive ions as illustrated in Fig. 8(b). As a result, the electrostatic field a_x is decreasing sharply from more than 50 to about 12 as shown in Fig. 8(d). Accordingly, the electron sheet *B* can continue to accelerate to ultrarelativistic velocity benefitting from the charge compensation effect of trajectory crossing as the Coulomb force decreases significantly after the crossing has occurred. The number density of the electron sheet *B* and the transverse field a_z before and after the crossing are shown in Figs. 8(c) and 8(e), where the number density $n_e \sim 680\, n_c$ of the combined electron sheets *A* and *C* that are represented by the blue elliptical dotted line, is much smaller than the number density $n_e \sim 1800\, n_c$ of electron sheet *B*. Also, the

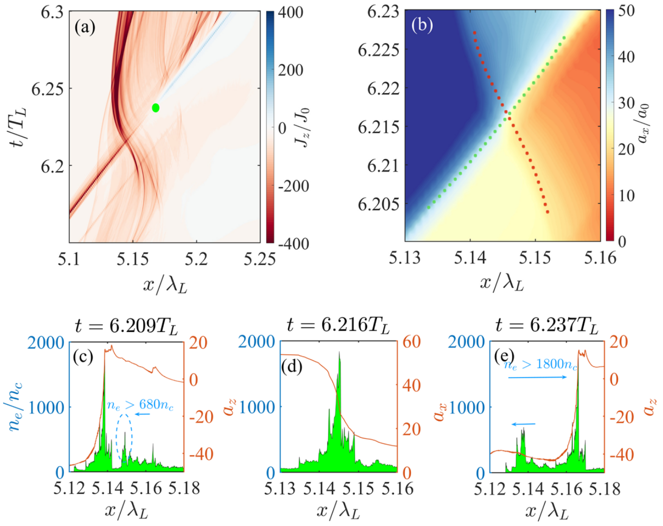

FIG. 8. The generation mechanism of the attosecond pulse in transmission direction. (a) The transverse current density, normalized by $j_0 = n_c e c$. The evolution near the SPP is highlighted by a green dot. (b) The longitudinal electric field $a_x = eE_x/(\omega_L m_e c)$ distribution near the SPP. The green and red dotted lines represent the trajectories of the electron sheet B moving towards the transmission direction and the electron sheets A and C towards the reflection direction, respectively. (c)–(e) The electron density n_e, transverse electric field a_z, and longitudinal electric field a_x before and after the crossing. Times $t = 6.216\,T_L$ and $t = 6.237\,T_L$ correspond to the moments of crossing and SPP, respectively.

longitudinal velocity of the combined electron sheets A and C is much smaller than that of electron sheet B from Figs. 3(a) and 3(b). The resulting intensity of the attosecond pulse in transmission direction is much larger than that in the reflected direction.

The transverse dynamics of the electron sheet B is governed by the momentum equation

$$\frac{d(\gamma v_z)}{dt} = -2\pi(a_z + v_x B_y), \tag{1}$$

where the electric field a_z, magnetic field B_y, and velocity (v_x, v_z) are normalized by $m_e\omega_L c/e$, $m_e\omega_L/e$ and c, respectively, and time t is normalized by λ_L/c. We will approximate $a_z \approx v_x B_y$ since the electron sheet B at the SPP has an ultrarelativistic longitudinal velocity $v_x \sim c$. The momentum equation can then be simplified as

$$\frac{d(\gamma v_z)}{dt} = -4\pi a_z. \tag{2}$$

From Fig. 9(b), the transverse electric field a_z in the vicinity of the SPP can be written $a_z \approx \kappa_0 t^2 + E_0$, where the coefficient $\kappa_0 = 8.359 \times 10^5$ and the constant term $E_0 = 11.006$ are determined from a quadratic fitting to the simulation result. As the low frequency band is filtered by the third target layer, we will pay attention to the high-frequency band of the spectrum of the transmitted radiation. Then we only consider the first term $\kappa_0 t^2$ of a_z. Accordingly, we can derive the transverse velocity $v_z = -\alpha_0 t^3$ with $\alpha_0 = (4\pi/3)(\kappa_0/\gamma_0)$ in the first-order approximation $\gamma \approx \gamma_0$. The normalized (by $en_c c$) transverse current $J_z(x, t) = -v_z(t)n[x - x_0(t)]$ is obtained as

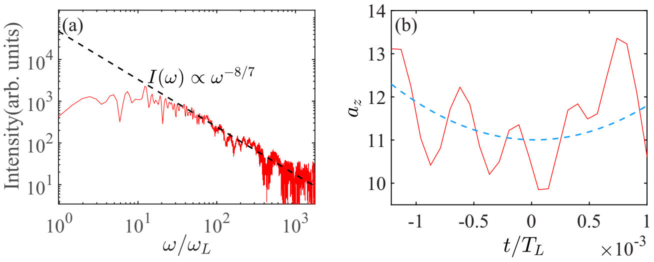

FIG. 9. (a) The harmonic spectra of the transmitted isolated attosecond pulse radiation behind the target. The attenuation of high-frequency band of the spectrum follows $I(\omega) \propto \omega^{-8/7}$. (b) The transverse electric field a_z in the vicinity of the SPP is shown by red line. The green line indicates the result of quadratic curve fitting, which shows that a_z can be approximately regarded as a parabola with time t.

$$J_z(x, t) = \alpha_0 t^3 n[x - x_0(t)], \tag{3}$$

which is consistent with that the transverse current direction changes from negative to positive at the SPP as shown in Fig. 8(a). Here, the position $x_0(t)$ of the electron sheet B can be determined from $v = (\dot{x}_0^2 + v_z^2)^{1/2}$ as $x_0(t) = vt - (\alpha_0/2v)(t^7/7)$, where v is the speed of the sheet normalized by c. The transmitted radiation electric field can be obtained from $E_T(t) = \pi \int J_z(x, t + x)\mathrm{d}x$ [32]. With the help of Eq. (3) and the position $x_0(t)$ of the electron sheet B, the transmitted radiation electric field can be clearly expressed by

$$E_T(t) = \pi \int \alpha_0(t + x)^3 n_e[x - x_0(t + x)]dx. \tag{4}$$

The Fourier transform of Eq. (4) can be written as $E_T(\omega) = \pi \iint \alpha_0(t + x)^3 n_e[x - x_0(t + x)]e^{-i\omega t}dxdt$. By using the variable substitution $t + x \to t'$ and the relationship $dt' = dt$, the Fourier transform of Eq. (4) can be written in the form

$$E_T(\omega) = \pi \int n_e(\xi)e^{i\omega\xi}d\xi \int \alpha_0 t'^3 e^{-i\omega[t' - x_0(t')]}dt', \tag{5}$$

where we introduced $\xi = x - x_0(t')$. The spectrum $I = |E_T(\omega)|^2$ of the transmitted attosecond pulse can be written as [32]

$$I(\omega) = 4\pi^4\alpha_0^2(\alpha_1\omega)^{-\frac{8}{7}}|\mathrm{Ai}_3'''(\xi)|^2|\widetilde{n}(\omega)|^2, \tag{6}$$

where $\alpha_1 = \alpha_0^2/2v$, $\xi = (1 - v)\omega^{\frac{6}{7}}\alpha_1^{-\frac{1}{7}}$, and $\mathrm{Ai}_3'''(\xi) = (1/2\pi)\int \tau^3 e^{i\xi\tau}e^{i\tau^7/7}d\tau$ is the third derivative of the generalized Airy function [32,33] of the third kind and $\widetilde{n}(\omega)$ is the Fourier transform of the density shape distribution of electron sheet B. The spectrum of HHG in the transmission direction in our simulation is shown in Fig. 9(a). It is seen that the above theoretical prediction confirms the $I(\omega) \propto \omega^{-8/7}$ scaling law for high frequencies in the spectrum. The transmitted radiation has a strong high-frequency component, which contributes to the emission of the ultrashort attosecond pulses. From the spectrum of forward attosecond pulse in Fig. 9(a), one can see that the central frequency is about $\nu = 10\omega_L/2\pi = 3.75 \times 10^{15}$ Hz, which means that the energy of the photon is about 15.53 eV.

Accordingly, the generated attosecond pulse can be useful for extreme-ultra-violet (XUV) pump-probe spectroscopy of ultrafast dynamics of electrons in the atoms, where the energy separation between the ground state and the first excited state is generally larger than 10 eV [34].

VI. ROBUSTNESS OF THE UNIQUE CSE REGIME

For the transmitted radiation, it is necessary to use at least a one-cycle driving laser pulse to ensure twice-per-cycle oscillation of the electron sheet. Only in this way can the electron sheet move in the direction of transmission. However, if we use one-cycle or multicycle driving laser pulse interacting on a thin nanofoil, the secondary electron sheet will be formed inevitably besides the primary electron sheet formed in the first half cycle of the laser pulse. The generation of this secondary electron sheet widely exists in the process of coherent synchrotron radiation. Both the primary electron sheet and secondary electron sheet will all contribute to the transmitted radiation. Accordingly, the attosecond pulses have two distinct subpulses and are temporally offset by 130 as [30]. In our unique CSE regime, the presence of the first target layer ensures that only one electron sheet contributes to the transmitted radiation.

The electrodynamics of the first target layer can be determined by the normalized areal charge density $\sigma_1 = 2\pi n_{e1} e^2 d_1 / m_e \omega_L c$ [35,36] with n_{e1} being the density and d_1 being the thickness of the first target layer. The expression of the normalized areal charge density can be written in another form as

$$\sigma_1 = \pi n_{e1} \frac{d_1}{\lambda_L}, \tag{7}$$

where n_{e1} is normalized by $n_c = m_e \omega_L^2 / 4\pi e^2$ and λ_L is the wavelength of a driven laser pulse. From the expression of σ_1 we can see that the first target layer will provide a similar background of positive charge when the product of density and thickness remains constant to ensure that the normalized areal charge density remains unchanged. One can also expect that the electrodynamics of the electron sheet will be similar when the density and thickness of the first layer target change simultaneously to ensure that their product $n_{e1} d_1$ is roughly unchanged.

We performed simulations to verify this mechanism, of which the simulation results are listed in Table I. The first column in the table shows that the thickness of the first target layer varies from 3 nm to 12 nm. The second column in the table shows that the density of the first target layer varies from $633 n_c$ to $159 n_c$. As the product of density n_{e1} and thickness d_1 remains roughly unchanged, the normalized areal charge density $\sigma_1 \sim 7.46$ for all cases. One can see from Table I that the durations are all below 10 as and the intensity $I > 8.5 \times 10^{20}\ \mathrm{W/cm^2}$ for all cases, which confirms that the unique CSE regime of attosecond pulse generation is always effective as long as the parameter σ_1 is roughly the same.

To intuitively prove that the physical mechanism of attosecond pulse generation is similar in all cases in Table I, the spatiotemporal evolution of the normalized electron number density n_e/n_c, the amplitude a_z, and intensity a_z^2 of the forward attosecond pulse is illustrated in Fig. 8. Since the physical processes of electron sheet formation and attosecond pulse generation in all cases are almost the same, we only show figures for three cases of them. The left column gives the case with $n_{e1} = 633 n_c$ and $d_1 = 3$ nm. The middle column gives the case with $n_{e1} = 317 n_c$ and $d_1 = 6$ nm. The right column gives the case with $n_{e1} = 211 n_c$ and $d_1 = 9$ nm. The intensity of the forward attosecond pulse will decrease with the increase of thickness of first target layer, as shown in Figs. 10(h) and 10(i), which is also confirmed from the third column of Table I. The formation dynamics of the electron sheet is almost identical in the three cases as shown in Figs. 10(a), 10(d), and 10(g), which are all very similar to that in Fig. 2(d). When the laser pulses penetrate vertically into the surface of the plasma, the electrons are compressed by the laser ponderomotive force to form the first electron sheet *A*. After that the second electron sheet *B* and the third sheet *C* are simultaneously formed. On one hand, the presence of the first target layer ensures that the combination of the Coulomb and Lorentz forces is strong enough that almost no electrons in the electron sheet *B* escape to a vacuum but instead return back to the transmission direction as shown in Figs. 10(a), 10(d), and 10(g). On the other hand, after crossing between electron sheet *B* and electron sheets *A* and *C* as shown in Figs. 10(a), 10(d), and 10(g), the electron sheets *A* and *C* will move in the reflection direction. Accordingly, the ultraintense isolated attosecond pulse in the transmission direction is only emitted by the electron sheet *B*.

TABLE I. The effect of the density and thickness of the first target layer on attosecond pulse generation with a normalized areal charge density $\sigma_1 \sim 7.46$ for all cases.

d_1(nm)	n_{e1}	FWHM(as)	a_z	$I(\times 10^{21}\ \mathrm{W/cm^2})$
3	633	4.9	−32.37	2.24
4	475	4.0	−32.61	2.27
5	380	3.5	−30.40	1.97
6	317	3.8	−32.64	2.27
7	271	3.2	−32.00	2.19
8	238	3.4	−27.15	1.57
9	211	4.4	−25.40	1.38
10	190	5.0	−20.36	0.88
11	172	3.8	−20.64	0.91
12	159	4.0	−19.91	0.85

We discuss the possible feasibility of realizing this microstructured target regime. The first target layer can be made by diamond-like carbon (DLC) foil [37], of which the thickness can be as small as 2.9 nanometers and the electron number density is about $311 n_c$ [38]. From Table I, the case of $d_1 = 6$ nm and $n_e = 317 n_c$ may be realized by the DLC foil. Behind the DLC, ultrathin gold foils with nanoholes (NH) may meet the thickness and density requirements of the second layer target by adjusting the size of the nanospheres [39]. As discussed above, the formation and dynamics of electron sheets *A*, *B*, and *C* have nothing to do with the third target layer that only acts as a high-pass filter. It was confirmed in Figs. 4(g), 4(h), and 4(i), where the dynamics of the formation of electron sheets B''', A''', and C''' without the third target layer are almost the same as the case with third target layer.

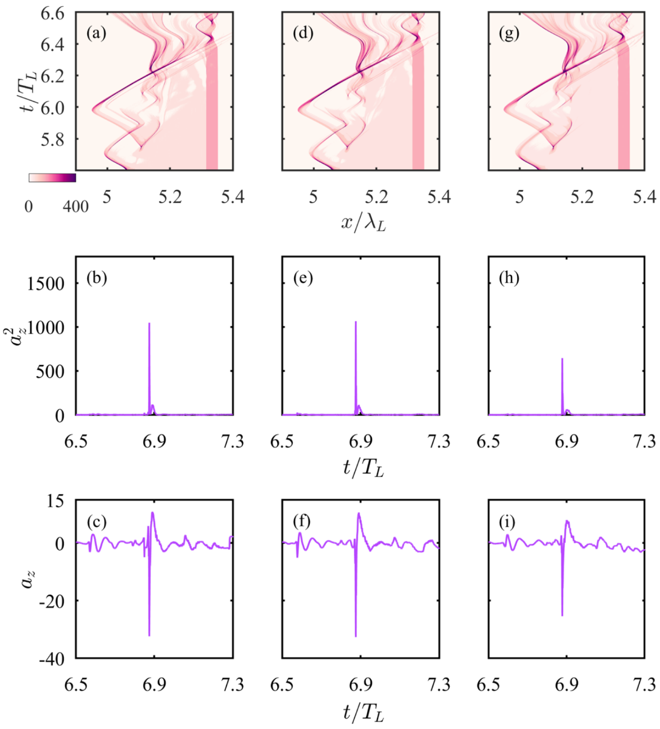

FIG. 10. The left column gives the case with $n_e = 633n_c$ and $d_1 = 3$ nm. The middle column gives the case with $n_e = 317n_c$ and $d_1 = 6$ nm. The right column gives the case with $n_e = 211n_c$ and $d_1 = 9$ nm. The first row gives spatiotemporal evolution of the normalized electron number density n_{e1}/n_c. The second row illustrates the intensity a_z^2 of attosecond pulse without filtering in transmission direction. The third row shows the electric field a_z profile of the attosecond pulses, which shows a half-cycle profile for the three cases.

The minor disadvantage of no third layer target is that a subpulse with very low intensity appears far away from the main attosecond pulse. Accordingly, the first target layer and second target layer play a crucial role in the unique CSE regime. The microstructured target only with the first and second target layers may be realized with present technology. The three-layer target is expected to be realized in the future.

VII. CONCLUSION

In summary, two-color laser pulses interacting with microstructured foils is an efficient way to directly generate ultraintense isolated attosecond pulses in the transmission direction by the CSE mechanism without the need for extra filters and gating techniques. In our electron nanobunching mechanism, only one electron sheet B from the second target layer contributes to the transmitted radiation, benefitting from the the presence of the first target layer. The resulting attosecond pulse does not have distinct subpulses, but instead one isolated attosecond pulse.

The electrodynamics of the electron sheets will be similar when the density and thickness of the first layer target changes simultaneously to ensure that their product $n_{e1}d_1$ is kept unchanged. As the first target layer provides a dense background of positive charge, the combination of the Coulomb and Lorentz forces is strong enough that almost no electrons in the electron sheet B [cf. Figs. 2(d) and 10(a), 10(d), and 10(g)] escape to a vacuum, but instead return back to the transmission direction and contribute to increasing sheet B to an ultrahigh electron number density. The electron sheet B continues to accelerate to ultrarelativistic longitudinal velocity at the SPP due to the charge compensation effect of electron sheet A whose electrons are almost all from the first target layer. The robustness of this unique CSE regime is verified by changing the plasma parameters and the relative phase between the two driving color laser pulses. In the unique microstructured foil regime, the attosecond pulse generation in the transmission direction is always effective as long as the normalized areal charge density σ_1 is roughly the same. The forward attosecond pulses are generated for a broad range of an energy ratio $\eta \sim 0.3$–0.7 of the two-color laser pulses with parallel linear polarization. The amplitude of the attosecond pulse decreases rapidly with the increase of relative phase between the two-color laser pulses with orthogonal linear polarization.

ACKNOWLEDGMENTS

This research is supported by National Natural Science Foundation of China (NSFC) (Grants No. 11974043 and No. 51861145309) and the Fundamental Research Funds for the Central Universities (Grant No. FRF-BR-19-002B). X.Y. acknowledges support by National Natural Science Foundation of China (Grant No. 11921006) and the National Grand Instrument Project (Grant No. 2019YFF01014400). The work by B.E. was carried out partially within the framework of the EUROfusion Consortium. We acknowledge useful discussions with Dr. Y. R. Shou. The data that support the results of this study are available upon request from the authors.

---

[1] T. Pfeifer, C. Spielmann, and G. Gerber, Rep. Prog. Phys. **69**, 443 (2006).

[2] M. V. Arkhipov, R. M. Arkhipov, A. V. Pakhomov, I. V. Babushkin, A. Demircan, U. Morgner, and N. N. Rosanov, Opt. Lett. **42**, 2189 (2017).

[3] A. S. Moskalenko, Z.-G. Zhu, and J. Berakdar, Phys. Rep. **672**, 1 (2017).

[4] I. Thiele, E. Siminos, and T. Fülöp, Phys. Rev. Lett. **122**, 104803 (2019).

[5] Y. Jiang, Z.-Y. Chen, Z. Liu, L. Cao, C. Zheng, R. Xie, Y. Chao, and X. He, Opt. Lett. **46**, 1285 (2021).

[6] Y. Shou, R. Hu, Z. Gong, J. Yu, J. Chen, G. Mourou, X. Yan, and W. Ma, New J. Phys. **23**, 053003 (2021).

[7] F. Y. Li, Z. M. Sheng, M. Chen, L. L. Yu, J. Meyer-ter-Vehn, W. B. Mori, and J. Zhang, Phys. Rev. E **90**, 043104 (2014).

[8] C. Thaury, F. Quéré, J.-P. Geindre, A. Levy, T. Ceccotti, P. Monot, M. Bougeard, F. Réau, P. d'Oliveira, P. Audebert, R. Marjoribanks, and P. Martin, Nat. Phys. **3**, 424 (2007).

[9] F. Quéré, C. Thaury, P. Monot, S. Dobosz, P. Martin, J.-P. Geindre, and P. Audebert, Phys. Rev. Lett. **96**, 125004 (2006).

[10] S. Gordienko, A. Pukhov, O. Shorokhov, and T. Baeva, Phys. Rev. Lett. **93**, 115002 (2004).

[11] B. Dromey, M. Zepf, A. Gopal, K. Lancaster, M. S. Wei, K. Krushelnick, M. Tatarakis, N. Vakakis, S. Moustaizis, R. Kodama, M. Tampo, C. Stoeckl, R. Clarke, H. Habara, D. Neely, S. Karsch, and P. Norreys, Nat. Phys. **2**, 456 (2006).

[12] B. Dromey, S. Kar, C. Bellei, D. C. Carroll, R. J. Clarke, J. S. Green, S. Kneip, K. Markey, S. R. Nagel, P. T. Simpson, L. Willingale, P. McKenna, D. Neely, Z. Najmudin, K. Krushelnick, P. A. Norreys, and M. Zepf, Phys. Rev. Lett. **99**, 085001 (2007).

[13] T. Baeva, S. Gordienko, and A. Pukhov, Phys. Rev. E **74**, 046404 (2006).

[14] P. Heissler, R. Hörlein, J. M. Mikhailova, L. Waldecker, P. Tzallas, A. Buck, K. Schmid, C. M. S. Sears, F. Krausz, L. Veisz, M. Zepf, and G. D. Tsakiris, Phys. Rev. Lett. **108**, 235003 (2012).

[15] D. an der Brügge and A. Pukhov, Phys. Plasmas **17**, 033110 (2010).

[16] J. M. Mikhailova, M. V. Fedorov, N. Karpowicz, P. Gibbon, V. T. Platonenko, A. M. Zheltikov, and F. Krausz, Phys. Rev. Lett. **109**, 245005 (2012).

[17] B. Dromey, S. Rykovanov, M. Yeung, R. Hörlein, D. Jung, D. C. Gautier, T. Dzelzainis, D. Kiefer, S. Palaniyppan, R. Shah, J. Schreiber, H. Ruhl, J. C. Fernandez, C. L. S. Lewis, M. Zepf, and B. M. Hegelich, Nat. Phys. **8**, 804 (2012).

[18] M. Yeung, B. Dromey, S. Cousens, T. Dzelzainis, D. Kiefer, J. Schreiber, J. H. Bin, W. Ma, C. Kreuzer, J. Meyer-ter-Vehn, M. J. V. Streeter, P. S. Foster, S. Rykovanov, and M. Zepf, Phys. Rev. Lett. **112**, 123902 (2014).

[19] M. Yeung, J. Bierbach, E. Eckner, S. Rykovanov, S. Kuschel, A. Sävert, M. Förster, C. Rödel, G. G. Paulus, S. Cousens, M. Coughlan, B. Dromey, and M. Zepf, Phys. Rev. Lett. **115**, 193903 (2015).

[20] C. Altucci, V. Tosa, and R. Velotta, Phys. Rev. A **75**, 061401(R) (2007).

[21] C. Altucci, R. Esposito, V. Tosa, and R. Velotta, Opt. Lett. **33**, 2943 (2008).

[22] C. Altucci, R. Velotta, V. Tosa, P. Villoresi, F. Frassetto, L. Poletto, C. Vozzi, F. Calegari, M. Negro, S. De Silvestri, and S. Stagira, Opt. Lett. **35**, 2798 (2010).

[23] Y. X. Zhang, S. Rykovanov, M. Shi, C. L. Zhong, X. T. He, B. Qiao, and M. Zepf, Phys. Rev. Lett. **124**, 114802 (2020).

[24] A. Tarasevitch and D. von der Linde, Eur. Phys. J.: Spec. Top. **175**, 35 (2009).

[25] S. Mirzanejad and M. Salehi, Phys. Rev. A **87**, 063815 (2013).

[26] M. R. Edwards, V. T. Platonenko, and J. M. Mikhailova, Opt. Lett. **39**, 6823 (2014).

[27] M. Yeung, S. Rykovanov, J. Bierbach, L. Li, E. Eckner, S. Kuschel, A. Woldegeorgis, C. Rödel, A. Sävert, G. G. Paulus, M. Coughlan, B. Dromey, and M. Zepf, Nat. Photonics **11**, 32 (2017).

[28] Z.-Y. Chen, Phys. Rev. E **97**, 043202 (2018).

[29] G. D. Tsakiris, K. Eidmann, J. Meyer-ter-Vehn, and F. Krausz, New J. Phys. **8**, 19 (2006).

[30] S. Cousens, B. Reville, B. Dromey, and M. Zepf, Phys. Rev. Lett. **116**, 083901 (2016).

[31] T. D. Arber, K. Bennett, C. S. Brady, A. Lawrence-Douglas, M. G. Ramsay, N. J. Sircombe, P. Gillies, R. G. Evans, H. Schmitz, A. R. Bell, and C. P. Ridgers, Plasma Phys. Control. Fusion **57**, 113001 (2015).

[32] M. Cherednychek and A. Pukhov, Phys. Plasmas **23**, 103301 (2016).

[33] D. an der Brügge and A. Pukhov, arXiv:1111.4133.

[34] F. Krausz and M. Ivanov, Rev. Mod. Phys. **81**, 163 (2009).

[35] V. A. Vshivkov, N. M. Naumova, F. Pegoraro, and S. V. Bulanov, Phys. Plasmas **5**, 2727 (1998).

[36] S. V. Bulanov, T. Zh. Esirkepov, M. Kando, S. S. Bulanov, S. G. Rykovanov, and F. Pegoraro, Phys. Plasmas **20**, 123114 (2013).

[37] W. J. Ma, V. K. Liechtenstein, J. Szerypo, D. Jung, P. Hilz, B. M. Hegelich, H. J. Maier, J. Schreiber, and D. Habs, Nucl. Instrum. Methods Phys. Res., Sect. A **655**, 53 (2011).

[38] A. Henig, S. Steinke, M. Schnürer, T. Sokollik, R. Hörlein, D. Kiefer, D. Jung, J. Schreiber, B. M. Hegelich, X. Q. Yan, J. Meyer-ter-Vehn, T. Tajima, P. V. Nickles, W. Sandner, and D. Habs, Phys. Rev. Lett. **103**, 245003 (2009).

[39] G. Cantono, A. Permogorov, J. Ferri, E. Smetanina, A. Dmitriev, A. Persson, T. Fülöp, and C.-G. Wahlström, Sci. Rep. **11**, 5006 (2021)